



# Study the multiferroic properties of $\text{BiFeO}_3/\text{Ni}_{0.1}\text{Fe}_{2.9}\text{O}_4$ for heavy metal removal

Rania Ramadan<sup>1</sup>

Received: 25 October 2022 / Accepted: 29 December 2022 / Published online: 17 January 2023  
© The Author(s) 2023

## Abstract

The important marvel in multiferroic substances is the existence of spontaneous polarization and magnetization which enable these materials meet the needs of technological applications. Multiferroic of  $\text{BiFeO}_3$  and nickel-doped magnetite was synthesized separately by flash and co-precipitation methods, respectively. The two phases were confirmed by X-ray diffraction (XRD), scanning electron microscope (SEM) and Fourier transformed infrared (FTIR) analysis. The dielectric properties of  $\text{BiFeO}_3/\text{Ni}_{0.1}\text{Fe}_{2.9}\text{O}_4$  nanocomposite were studied as a function of temperature as well as frequency. Based on the frequency dependent of ac conductivity results, it indicated that the conduction occurs through tunneling and small polaron hopping. The composite sample shows excellent results for heavy metal ( $\text{Cr}^{6+}$ ) removal from wastewater as the removal efficiency was reached to 75% at PH 6 after 40 min. The adsorption of Cr (VI) on the surface of nanocomposite was occurred through Langmuir isotherm and follows pseudo-second-order kinetics. The goal and novelty of this work were to investigate the structural, morphological and dielectric as well as magnetic properties of multiferroic nanocomposite material ( $\text{BiFeO}_3/\text{Ni}_{0.1}\text{Fe}_{2.9}\text{O}_4$ ) and test its efficiency for heavy metal removal.

**Keywords** Multiferroic ·  $\text{BiFeO}_3$  ·  $\text{Ni}_{0.1}\text{Fe}_{2.9}\text{O}_4$  · Ac conductivity · Magnetic susceptibility · Heavy metal removal · Langmuir isotherm · Kinetics

## 1 Introduction

Since the industrial revolution, the pollution of the environment has become a universal issue, especially in developing countries. It is known that, without water no mortal can live on earth, as the water is the most important resource for human creatures. Though, the dangerous environmental pollution threatens human health. The main sources of contaminants in water are heavy metals (metals which has atomic numbers larger than 20). Heavy metals commonly present as cations as  $\text{Cr(VI)}$ ,  $\text{Pb}^{2+}$ ,  $\text{Cd}^{2+}$ ,  $\text{As}^{3+}$ ,  $\text{Ag}^+$  or exist as anions (i.e., arsenate, arsenite, etc.). Heavy metals pollution has a serious effect on public health and environment, as they have the ability to accumulate in human body leading to life-threatening diseases. Usually physical, chemical and biological approaches have been used to remedy the heavy metals, biomaterials and organic contaminations from water.

The predictable techniques [1] for heavy metal remediation from water consist of adsorption [2, 3], chemical precipitation [4], membrane filtration [5] ion, ion exchange [6] and flotation and extraction [7]. Among these methods, the adsorption technique is the most efficient one, because it is an efficient and conventional technique for removing heavy metals from water [8–10]. The expansion of nanotechnology offers a promising replacement to improve the treatment efficiency. Consequently, NMs have attracted considerable interest for the finding and removal of heavy metals from water. Thus, the synthesis of NMs offers advancing opportunities for water purification and environmental sustainability [11]. Multiferroic materials show more than one of the properties of ferroelectric, ferromagnetic and ferroelastic in the same stage [12]. Multiferrocity (Magnetoelectricity) is a coexistence of magnetic and electric ordering in the same phase [13]. These materials have gained great attention for numerous applications as electronics [14], memory devices [15], sensors [16] and switches [17]. Magnetoelectricity in single-phase compounds displays intrinsic magnetoelectric coupling because of its homogeneity and chemically isotropic. Consequently, instantaneous existence of

✉ Rania Ramadan  
rramadan@sci.cu.edu.eg

<sup>1</sup> Materials Science Lab (1), Physics Department, Faculty of Science, Cairo University, Giza, Egypt

ferromagnetic as well as ferroelectric is required [18]. On other hand, single-phase sample suffers from low permeability or permittivity causing weak magnetoelectric coupling and obstructs their countless applications [19]. In the last years, hundreds of single-phase materials were studied; many attempts are being done to enhance the magnetoelectric coupling. For example, BiFeO<sub>3</sub> has antiferromagnetism ( $T_N \approx 640$  K) and ferroelectricity ( $T_c \approx 1100$  K) at room temperature [19]. Above room temperature, it shows high ferroelectric polarization, while ferromagnetic behavior is weak which causes weak magnetoelectric coupling effect [20]. Synthesis of nanocomposites overcomes these drawbacks of BiFeO<sub>3</sub> by combining ferromagnetic and ferroelectric materials [21]. As a result, it is expected that magnetoelectric effect of BFO can be enhanced by adding strong magnetic material as magnetite nanoparticles [Fe<sub>3</sub>O<sub>4</sub>] doping with Ni which has great magnetic properties [22].

In this text, it is the first time of adding BFO to Ni-doped magnetite to form BiFeO<sub>3</sub>/Ni<sub>0.1</sub>Fe<sub>2.9</sub>O<sub>4</sub> multiferroic nanocomposite. This multiferroic nanocomposite was prepared successfully. Detailed study of structure, morphology, electric and magnetic properties was carried out. By adding doped magnetite material to perovskite material, it is observed that the dielectric loss reduces. Making this composite promising for heavy metal removal (Cr<sup>2+</sup>). As it is expected that by adding BFO into Ni-doped magnetite (BiFeO<sub>3</sub>/Ni<sub>0.1</sub>Fe<sub>2.9</sub>O<sub>4</sub>) enhances the removal of Cr(VI) from the water.

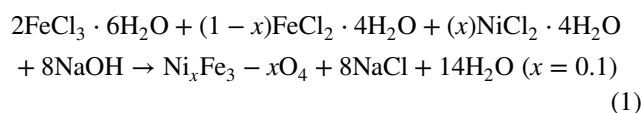
## 2 Methodology

### 2.1 Material used

Bismuth nitrate [Bi(NO<sub>3</sub>)<sub>3</sub>·5H<sub>2</sub>O], iron nitrate [Fe(NO<sub>3</sub>)<sub>3</sub>·9H<sub>2</sub>O] and urea [CH<sub>4</sub>N<sub>2</sub>O], ferric chloride hexahydrate (FeCl<sub>3</sub>·6H<sub>2</sub>O), ferrous chloride tetrahydrate (FeCl<sub>2</sub>·4H<sub>2</sub>O), nickel chloride tetrahydrate (NiCl<sub>2</sub>·4H<sub>2</sub>O). All chemicals are brought from LOBA, India (99.9% purity) and used without further purification.

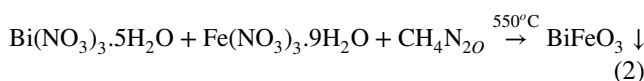
### 2.2 Synthesis of Ni<sub>0.1</sub>Fe<sub>2.9</sub>O<sub>4</sub> nanoparticles

Ni-doped magnetite was prepared by the co-precipitation process at 25 °C in air atmosphere. Proper amounts of (FeCl<sub>3</sub>·6H<sub>2</sub>O), (FeCl<sub>2</sub>·4H<sub>2</sub>O), (NiCl<sub>2</sub>·4H<sub>2</sub>O) were dissolved in distilled water to make a pure solution. After that, pH was attuned at 13 by using droplets of NaOH solution under continuous stirring. The solution changed from yellow toward black. The resultant solution was vigorous stirring for 15 min at 25 °C. The final precipitate was washed with distilled water and ethanol for several and then dried at 80 °C. This process can be expressed by this equation [23]:



### 2.3 Synthesis of Bi FeO<sub>3</sub> nanoparticles

The sample BiFeO<sub>3</sub> was prepared by flash method by mixing stoichiometric quantities of Bi(NO<sub>3</sub>)<sub>3</sub>·5H<sub>2</sub>O, Fe(NO<sub>3</sub>)<sub>3</sub>·9H<sub>2</sub>O and urea. Final powder was mixed well for 15 min. Then, temperature was elevated to 250 °C till all fumes were ended. The obtained powder was washed several times by distilled water and ethanol and then calcined for 2 h at 550 °C by rate of 5 °C/min. The reaction for the synthesis of Bi FeO<sub>3</sub> could be expressed as follows [24]:



### 2.4 Synthesis of Bi FeO<sub>3</sub>/Ni<sub>0.1</sub> Fe<sub>2.9</sub>O<sub>4</sub> multiferroic nanocomposite

Multiferroic nanocomposite Bi FeO<sub>3</sub>/Ni<sub>0.1</sub> Fe<sub>2.9</sub>O<sub>4</sub> was prepared by mixing stoichiometric amount of pure phase Bi FeO<sub>3</sub> and Ni<sub>0.1</sub> Fe<sub>2.9</sub>O<sub>4</sub> nanopowder about 1gm each by dry mechanical mixing at room temperature for 1 h after preparing each phase individually as mentioned above.

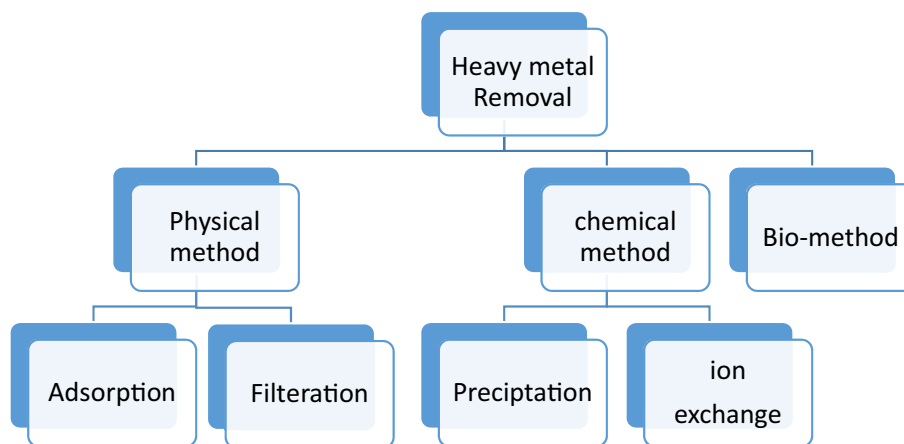
### 2.5 Characterizations and measurements

X-ray diffraction was carried out in the range of Bragg angles  $2\theta$  ( $20^\circ \leq 2\theta \leq 80^\circ$ ) for confirmation of single-phase formation of prepared sample. Fourier transform infrared spectroscopy (PerkinElmer 2000) was used for measuring FTIR spectra with wavelength range (4000–400) cm<sup>-1</sup>. The powder surfaces were scanned by using scanning electron microscope (SEM) [model: QUANTA-FEG250, Netherlands]. Gwyddion software (2.45) was used for investigating the topological characterization of prepared samples which were obtained from SEM. 3D image for each sample was obtained. Finally, the roughness parameters were calculated by using the same software. The magnetic properties were studied by using a homemade setup through Faraday's method at diverse magnetic field intensities. The electrical behavior of prepared samples was measured by LCR meter (Hioki 3532, Japan) from room temperature up to 650 K at different frequencies.

### 2.6 Batch experiment of heavy metal (Cr(VI)) removal

Many techniques are used for removal of heavy metals as shown in Fig. 1; the adsorption is the most preferred one

**Fig. 1** Methods for wastewater treatment of heavy metals



as mentioned above. The conduct experiment was carried out in 250-mL flasks with (0.1 g) of Bi FeO<sub>3</sub>/Ni<sub>0.1</sub> Fe<sub>2.9</sub>O<sub>4</sub> nanocomposite in 2 ppm of metals nitrate to determine the appropriate pH values for heavy metal (Cr(VI)) removal. PH solution was changed from 2 to 8. The examined solutions were fully mixed for 1 h at room temperature using an electric shaker (ORBITAL SHAKER SO1) at 200 rpm. Then, the solutions were collected using a 0.2-m syringe filter. At 25 °C, atomic absorption spectroscopy (Zeenite 700P, Analytical Jena) was used to determine the heavy metal concentration. Every experiment was repeated three times, with the average results reported.

The optimum contact time was observed by repeating the previous process while keeping the pH at its optimum value and measuring atomic absorption after various contact times (1–24 h). The heavy removal efficiency is calculated using the following formula [16].

$$\text{Removal(adsorption)efficiency}\% = \frac{C_0 - C_f}{C_0} \times 100\% \quad (3)$$

where C<sub>0</sub> : heavy metal soln at initial concentration (ppm), C<sub>f</sub> : heavy metal soln at final concentration (ppm).

### 3 Results and discussion

#### 3.1 X-ray diffraction

Figure 2 Comparing the XRD diagram with ICDD card no. [01-071-2494] and [01-087-2338] for BiFeO<sub>3</sub> and Ni<sub>0.1</sub>Fe<sub>2.9</sub>O<sub>4</sub>, respectively, indicating that, the individual nanosamples were prepared in a single-phase without any impurities form. The indexed peaks were related to the rhombohedral–hexagonal lattice with space group R3c for BFO, while it displayed a cubic structure with space group Fd3m for Ni-doped magnetite. Major peaks of nanocomposite represented the formation

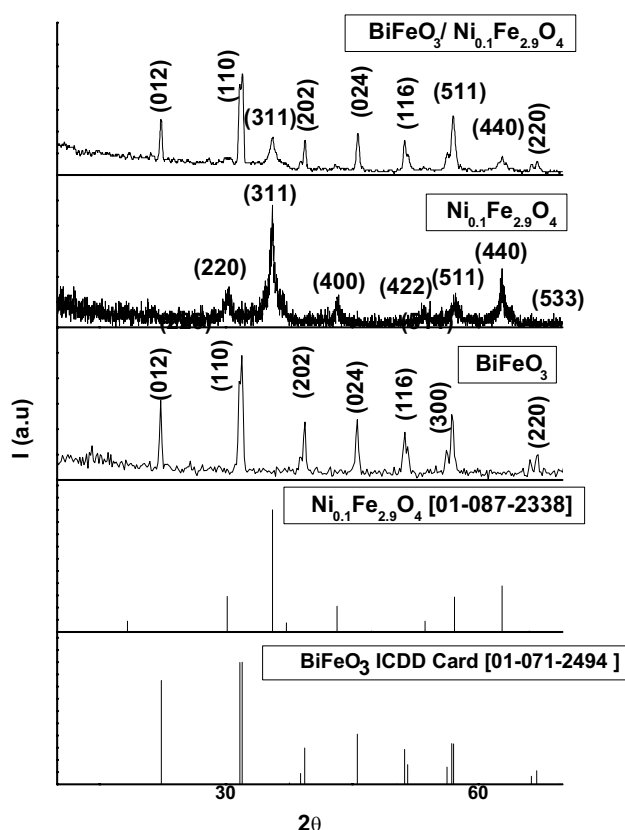


**Fig. 2** X-ray diffraction pattern of Bi FeO<sub>3</sub>, Ni<sub>0.1</sub> Fe<sub>2.9</sub>O<sub>4</sub> and Bi FeO<sub>3</sub>/Ni<sub>0.1</sub> Fe<sub>2.9</sub>O<sub>4</sub> multiferroic nanocomposite

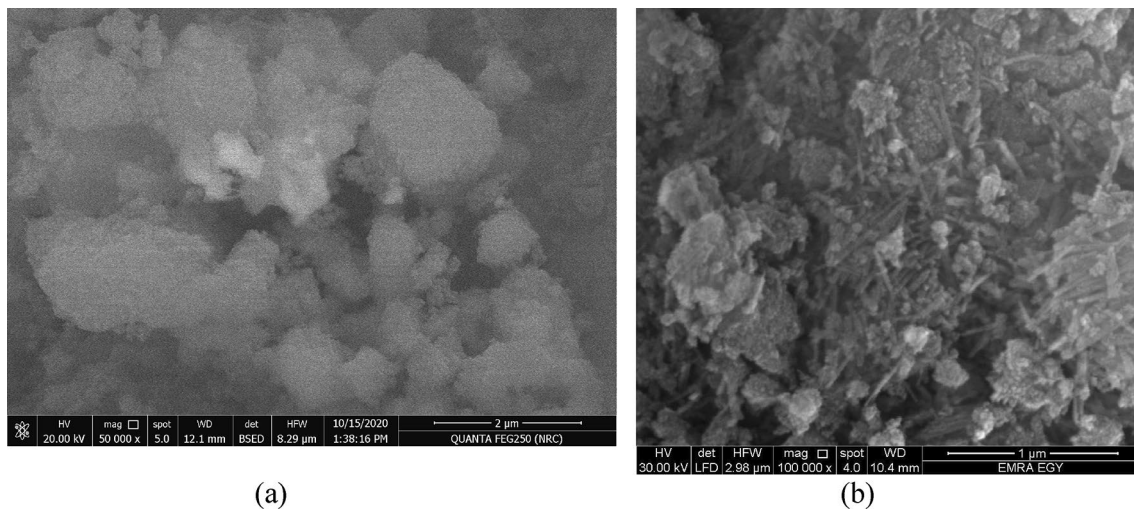
of diphases sample. Scherrer’s equation was used for calculating the average crystallite size [15].

$$D = \frac{k\lambda}{\beta_{hkl} \cos\theta} \quad (3)$$

where D is the crystallite size (nm), k is related to shape factor (0.9), λ is X-ray wavelength, and β<sub>hkl</sub> represents full

**Table 1** Crystallite size and lattice parameters of the prepared samples

Sample	Crystallite size (nm)	Calculated Lattice parameters			ICDD card Lattice parameters		
		A (Å)	b(Å)	c(Å)	a(Å)	b(Å)	c(Å)
BiFeO <sub>3</sub>	51.96	5.5818	5.58186	5.6441	5.5730	5.5730	6.9150
Ni <sub>0.1</sub> Fe <sub>2.9</sub> O <sub>4</sub>	8.3605	8.3604	8.3604	8.3604	8.3608	8.3608	8.3608
Bi FeO <sub>3</sub> /Ni <sub>0.1</sub> Fe <sub>2.9</sub> O <sub>4</sub>	76.11829	8.3502 5.58452 a for (Ni <sub>0.1</sub> Fe <sub>2.9</sub> O <sub>4</sub> )= 8.356871	8.3502	5.6441			

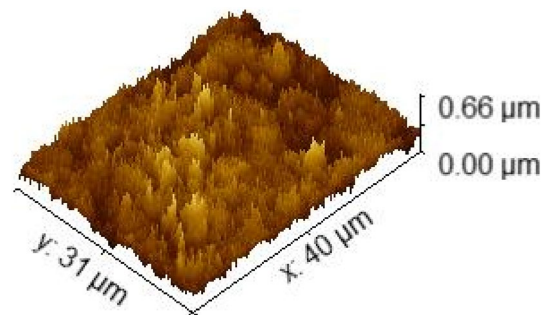
**Fig. 3** SEM microscopy of **a** Bi FeO<sub>3</sub> / Ni<sub>0.1</sub> Fe<sub>2.9</sub>O<sub>4</sub> nanocomposites and **b** Ni<sub>0.1</sub> Fe<sub>2.9</sub>O<sub>4</sub> nanoparticles

width at half maximum (FWHM). All lattice parameters as well as crystallite size were calculated and are listed in Table 1.

As shown in Table 1, there is a good agreement between the calculated lattice parameters and its theoretical values from ICDD cards. There is a small deviation in lattice parameters of nanocomposite Bi FeO<sub>3</sub>/Ni<sub>0.1</sub> Fe<sub>2.9</sub>O<sub>4</sub>, which may be related to minor distortion induced to sample or essential phases exerted stress on each other during single-phase mixing [16]

### 3.2 Morphological study of Bi FeO<sub>3</sub>/Ni<sub>0.1</sub> Fe<sub>2.9</sub>O<sub>4</sub> nanocomposite

Figure 3a displays SEM picture of Bi FeO<sub>3</sub>/Ni<sub>0.1</sub> Fe<sub>2.9</sub>O<sub>4</sub> nanocomposite. The morphologies of the obtained samples were dense in addition to the micrographs, and it is obvious that the grains are arbitrarily oriented and distributed over the whole sample; there is also a combination between two dissimilar grain sizes. BFO with different rhombohedral structures, as the small-scale BiFeO<sub>3</sub>

**Fig. 4** 3D micrographs of Bi FeO<sub>3</sub>/Ni<sub>0.1</sub> Fe<sub>2.9</sub>O<sub>4</sub> nanocomposite

crystallites gather into larger particles with irregular shape. While small size distribution related to Ni<sub>0.1</sub> Fe<sub>2.9</sub>O<sub>4</sub> Fig. 3b.

Figure 4 shows the surface roughness of Bi FeO<sub>3</sub>/Ni<sub>0.1</sub> Fe<sub>2.9</sub>O<sub>4</sub> nanocomposites. The surface roughness was studied through the roughness average which is defined as average, or arithmetic average of profile height deviations from the mean line and given by equation

$$R_a = \frac{1}{l} \int_0^l |Z(x)| dx \tag{4}$$

where  $R_a$  is the average roughness,  $l$  is sample length and  $Z(x)$  = profile ordinates of roughness profile.

While the root mean square roughness ( $R_q$ ) is the root mean square average of the roughness profile ordinates and given by

$$R_q = \sqrt{\frac{1}{l} \int_0^l |Z(x)|^2 dx} \tag{5}$$

Also, the maximum height of roughness was obtained by using Gwyddion software (2.45), and it is defined as total height of the roughness profile: Sum from the height ( $Z_p$ ) of the highest profile peak and the depth ( $Z_v$ ) of the lowest profile valley within the evaluation length. And given by

$$R_t = Z_p + Z_v \tag{6}$$

where  $R_t$  is the maximum height, ( $Z_p$ ) is the highest profile peak, and depth ( $Z_v$ ) is the lowest profile valley.

As it obtained from Table 2, all roughness parameters show high values. Consequently, this prepared sample is suitable for the desired applications as photocatalysis and heavy metal removal as the roughness in surface acts as trapping sites.

### 3.3 Dielectric properties

Figure 5a, b shows the variation of dielectric constant as well as dielectric loss as a function of temperature for different frequencies range (100 K–4 M) Hz. From the figure, it is clear that both dielectric constant and dielectric loss follow same trend. As temperature increases, value of  $\epsilon'$  and  $\epsilon''$  increases. This is may be attributed to thermal energy, at low temperature, thermal energy is not sufficient enough to liberate localized dipoles. By increasing temperature thermal energy, orient dipoles easily in the field direction. The dependence of dielectric constant on frequency is observed in figure below. As the dielectric constant has high value in low frequency range and its low value is corresponding to higher frequency range. Because dielectric behavior at low frequency is related to electronic, atomic, ionic and interfacial polarization, while, in high frequency, only electronic and ionic polarization is dominated. This behavior can be

**Table 2** Roughness parameters (roughness average  $R_a$ , root mean square roughness  $R_q$ , maximum height of roughness  $R_t$ ) of Bi FeO<sub>3</sub>/Ni<sub>0.1</sub> Fe<sub>2.9</sub>O<sub>4</sub> nanocomposite

$R_a$ (nm)	$R_q$ (nm)	$R_t$ (nm)
254.4	69.56	413.4

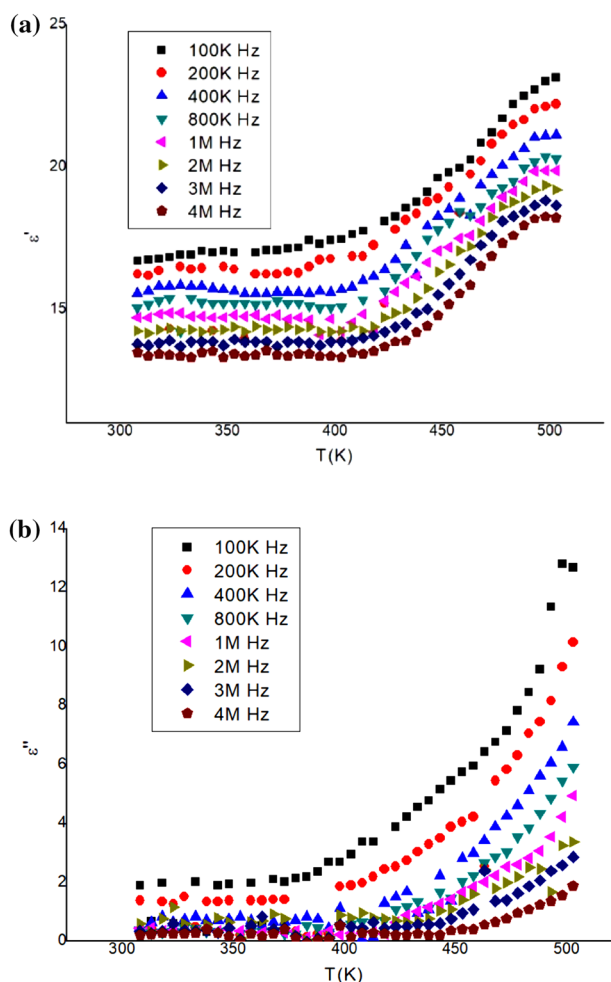


**Fig. 5** Relation between **a** dielectric constant and **b** dielectric loss as a function of temperature at different frequency range

explained by Koop's model [16], for dielectric material. It has two layers good (grains) and poor (grains boundary) conductive layers. At low frequency, charges are aggregated at boundary as a result, the value of capacitance increased and dielectric constant value increased. More conducting grains were existed by increasing frequency. So, less energy is required for hopping process. Consequently, value of dielectric constant decreased [17]. The value of dielectric constant for pure BiFeO<sub>3</sub> is a round 30 which related to large number of electrons hopping between Fe<sup>2+</sup> & Fe<sup>3+</sup> ions [18] while, for Ni<sub>0.1</sub>Fe<sub>2.9</sub>O<sub>4</sub> is about 15 [19] because of small amount of hopping electrons. Herein, the prepared nanocomposite shows dielectric constant value in between of its parent.

As shown in Fig. 5, at the low temperature, the conductivity is nearly constant and then began increasing with increasing temperature. This behavior is similar to the semiconductor materials [20]. The conduction mechanism at the beginning is related to impurities and structure defects



while, by heating  $Fe^{2+}$  is formed and easily transformed to  $Fe^{3+}$ , as a result conductivity is enhanced due to intrinsic conduction. Ac conductivity is increasing by increasing frequency range. As numbers of small polaron between states increased by increasing frequency [21]. Activation energy of prepared sample can be calculated from Arrhenius equation [22]:

$$\sigma = \sigma_0 \exp(-E/kT) \tag{7}$$

where  $E$ : activation energy,  $k$  Boltzmann`s constant,  $T$  absolute temperature

From Fig. 6b, it is observed that there are different conduction mechanisms. As there is different slopes of conductivity versus temperature. The values of activation energy are 0.25 eV and 0.61 eV for low and high temperature range, respectively. Conduction mechanisms may be related to small polaron tunneling at low range temperature while related to barrier hopping between  $Fe^{2+}$   $Fe^{3+}$  at high temperature range [23]

### 3.4 Magnetic study

Figure 7 shows the magnetic molar susceptibility as a function of temperature for different values of magnetic field intensities of BFO-Ni-doped magnetite nanocomposite. It is clear that  $\chi_M$  decreases as temperature as well as field intensity increases. By increasing magnetic field intensity, the alignment of dipoles along field direction is increasing in other hand, because of rising temperature, thermal energy increases dipoles disorder, and as a result, magnetic susceptibility decreases gradually until reaching zero (Curie temperature) [24–26].

The obtained data obtained from Fig. 8 fit well Curie–Weiss law as reciprocal of molar susceptibility

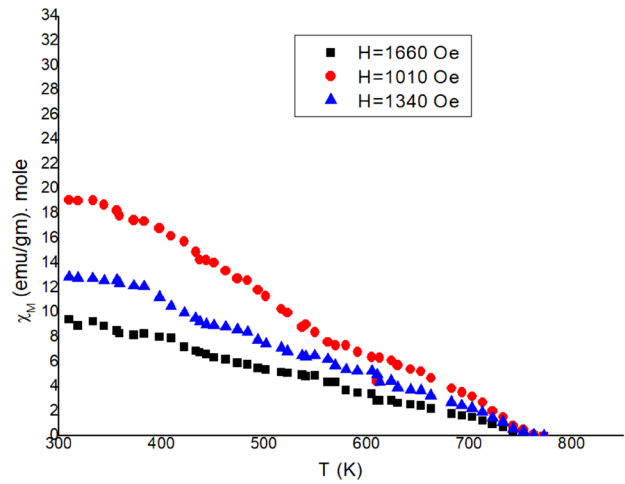


Fig. 7 Molar magnetic susceptibility as a function of temperature for different field intensities of  $BiFeO_3-Ni_{0.1}Fe_{2.9}O_4$  nanocomposite

directly proportional with temperature in paramagnetic region. The effective magnetic moment is calculated from the following equation [27]:

$$\mu_{eff} = 2.83\sqrt{C} \tag{8}$$

where  $C$  is curie constant.

Curie–Weiss constant ( $\theta$ ), curie constant ( $c$ ), and effective magnetic moment are calculated from Fig. 7 and listed in Table 3.

From the previous data, we noticed that nanocomposite sample has a ferromagnetic behavior despite, the antiferromagnetic nature of pure BFO. The enhancement of magnetic properties may be referring to interaction of dipoles between interface boundaries of ferromagnetic ( $Ni_{0.1}Fe_{2.9}O_4$ ) and antiferromagnetic (BFO). The net magnetization is related

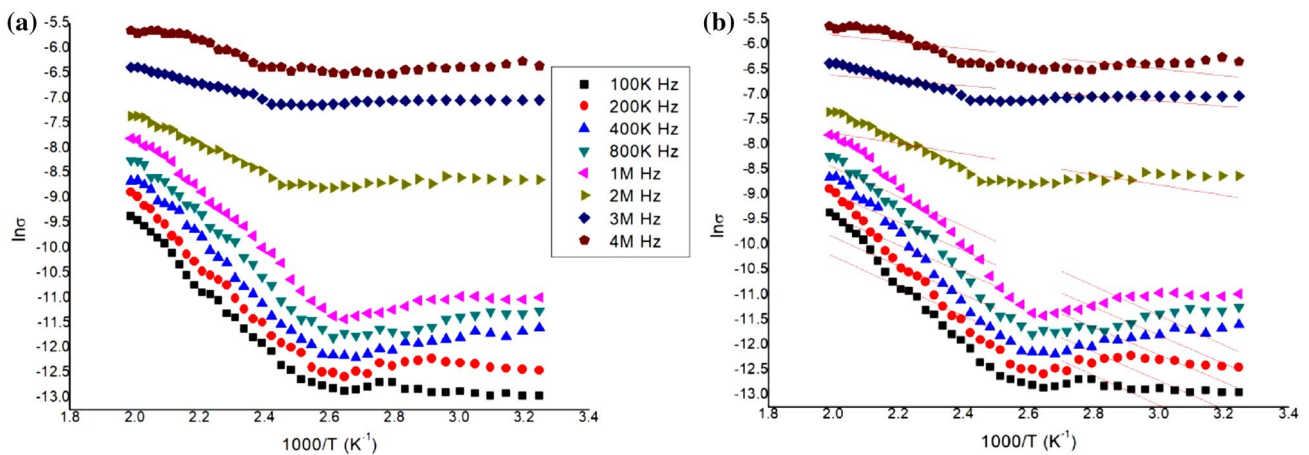
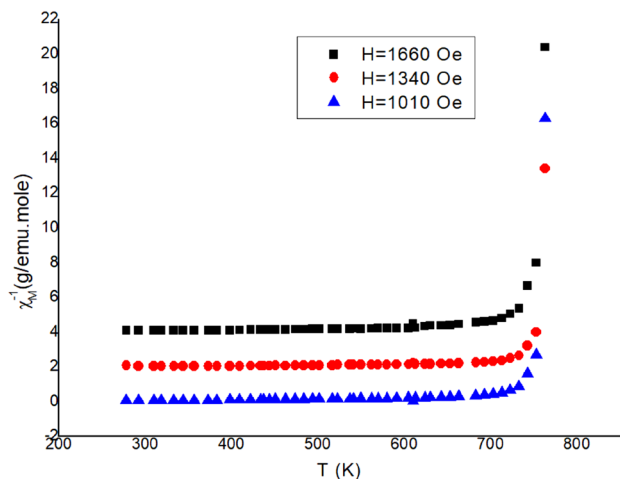


Fig. 6 a Relation between  $\ln \sigma$  and reciprocal of temperature ( $1000/T$ ), b the fitting curve



**Fig. 8** Reciprocal of molar magnetic susceptibility as a function of temperature for different field intensities of BiFeO<sub>3</sub>-Ni<sub>0.1</sub>Fe<sub>2.9</sub>O<sub>4</sub> nanocomposite

**Table 3** Magnetic constants of Curie-Weiss constant ( $\theta$ ), curie constant ( $c$ ), and effective magnetic

H(Oe)	$T_c$ (K)	(K) $\theta$	C (emu.mole.K/g)	$\mu_{\text{eff}}$ (B.M)
1010	762	745	166.6667	36.53514
1340	765	748	232.5581	43.1571
1660	760	752	142.8571	33.82497

to addition or subtraction of (BFO and Ni<sub>0.1</sub>Fe<sub>2.9</sub>O<sub>4</sub>) dipoles moment which have the same or opposite directions, respectively. Herein, the magnetic properties of the BiFeO<sub>3</sub> are improved successfully by making composite with Ni-doped magnetite.

### 3.5 Batch experiment

#### 3.5.1 Effect of experimental parameters (pH and contact time on heavy metal removal)

The up-taking behavior of Cr (VI) ions by BiFeO<sub>3</sub>-Ni<sub>0.1</sub>Fe<sub>2.9</sub>O<sub>4</sub> nanocomposites was examined at different pH and contact time. Figure 9 displays adsorption behavior at different pH values. It is clear that the removal efficiency of BiFeO<sub>3</sub>-Ni<sub>0.1</sub>Fe<sub>2.9</sub>O<sub>4</sub> nanocomposites for Cr (VI) increases as pH increases. The lower value of heavy metal removal at lower pH value related to competition between H<sup>+</sup> and Cr<sup>6+</sup> over the available active sites of adsorbent [28]. While pH value increased up to 7 and this is associated with decreasing H<sup>+</sup>, and as a result, more active sites become available for Cr (VI) adsorption [29]. On other hand, at basic medium [pH = 8], OH<sup>-</sup> ions exist in solution. Consequently, Cr (OH)<sub>6</sub> is formed [30]. So,

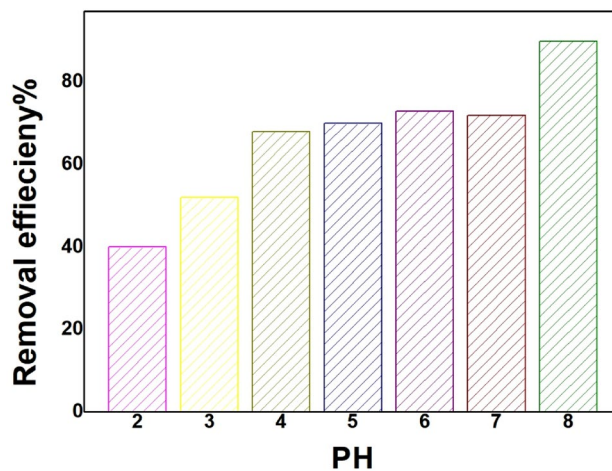


**Fig. 9** Removal efficiency % of BiFeO<sub>3</sub>-Ni<sub>0.1</sub>Fe<sub>2.9</sub>O<sub>4</sub> nanocomposites at different pH values

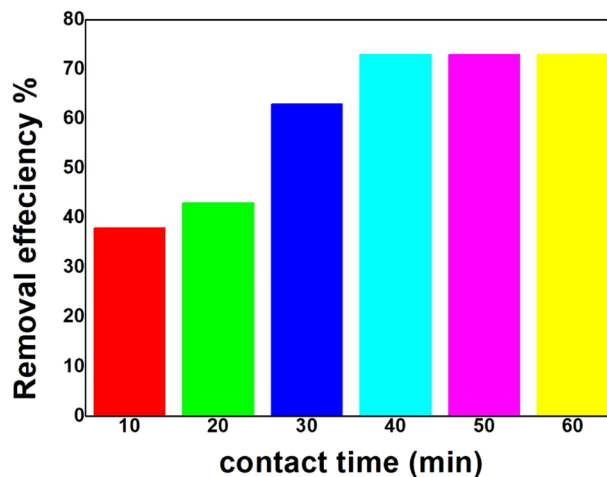


**Fig. 10** Removal efficiency % of BiFeO<sub>3</sub>-Ni<sub>0.1</sub>Fe<sub>2.9</sub>O<sub>4</sub> nanocomposites

removal of Cr(VI) ions was associated with adsorption as well as precipitation. So, the optimal pH was preferred to be 6.

From Fig. 10, it is obvious that removal efficiency of BiFeO<sub>3</sub>-Ni<sub>0.1</sub>Fe<sub>2.9</sub>O<sub>4</sub> nanocomposite increased as contact time increased. At the beginning, there are massive no of active sites for adsorption [31]. Removal efficiency for Cr (VI) by using the maximum adsorption of BiFeO<sub>3</sub>-Ni<sub>0.1</sub>Fe<sub>2.9</sub>O<sub>4</sub> nanocomposite reached to 75% after 60 min. Finally, the optimum conditions were determined for adsorption of Cr (VI) for pH 6 and contact time 60 min.

Isotherm and kinetics study.

Figure 11a, b displays Langmuir and Freundlich adsorption isotherms [32]. Langmuir and Freundlich isotherms are given by Eq. (6) and (7), respectively.

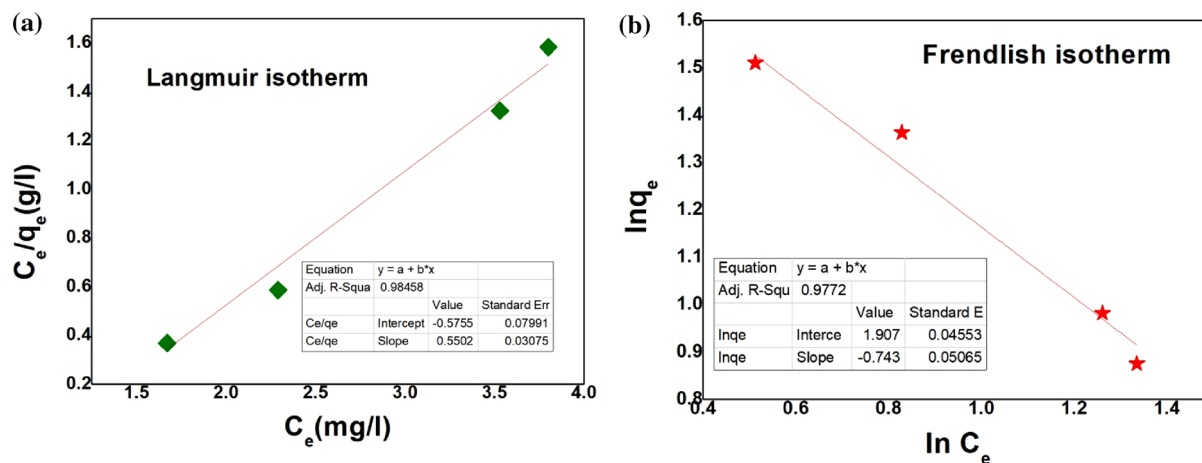


**Fig. 11** **a** Langmuir isotherm and **b** Freundlich isotherm for  $\text{BiFeO}_3\text{-Ni}_{0.1}\text{Fe}_{2.9}\text{O}_4$  nanocomposite

$$\frac{C_e}{q_e} = \frac{1}{k_f q_m} + \frac{C_e}{q_m} \quad (9)$$

$$\ln q_e = \ln k_f + \frac{1}{n} \ln C_e \quad (10)$$

where  $q_e$  and  $q_m$  ( $\text{mg g}^{-1}$ ) are the adsorption capacity at equilibrium and maximum adsorption, respectively, and  $K_l$  ( $\text{L mg}^{-1}$ ) is the affinity binding constant, while  $K_f$  and  $n$  are physical constants signifying the adsorption capacity and intensity of adsorption, respectively.

The Langmuir isotherm is related to monolayer adsorption at comparable sites and similar adsorption energies [25]. Although, Freundlich isotherm is attributed to dissimilar surfaces [32]. From Fig. 11a, b, it is noticed that the data are more fitting to Langmuir model, and from another point of view, the correlation coefficient ( $R^2$ ) for Langmuir (0.9899) is greater than that for Freundlich (0.9772). Therefore, adsorption of Cr (VI) on  $\text{BiFeO}_3\text{-Ni}_{0.1}\text{Fe}_{2.9}\text{O}_4$  nanocomposite surface followed monolayer adsorption.

To study the mechanism of the adsorption kinetic, three models were applied:

$$\text{Pseudo - first - order model : } \ln(q_e - q_t) = \ln q_e - \frac{k_1}{2.303} t \quad (11)$$

$$\text{Pseudo - second - order model : } \frac{t}{q_t} = \frac{1}{k_2 q_e^2} + \frac{t}{q_e} \quad (12)$$

$$\text{Inter - particle diffusion model } q_t = k_3 t^{1/2} + C \quad (13)$$

where  $k_1$ ,  $k_2$  and  $k_3$  are the pseudo-first, second-order and inter-particle diffusion rate constants in ( $\text{min}^{-1}$ ) and ( $\text{g mg}^{-1} \text{min}^{-1}$ ), respectively.

Pseudo-first-order kinetics is related to the physisorption. Physisorption is weak as it occurs without chemical bonding, just van der Waals forces occur. Accordingly, this adsorption is believed to be reversible. However, pseudo-second-order kinetic trades with chemisorption adsorption which is transpired through two reactions. Initial reaction, it extends equilibrium quickly. While another reaction reveals slowly and reaches equilibrium after long time [27]. In chemisorption, there is bond formation between adsorbates and adsorbents across electron sharing. Hence, it is stronger than physisorption. One more type of kinetic models is the intra-particle diffusion kinetic model. Weber and Morris model is studying this type of kinetic, which assumes that intra-particle diffusion model is the single rate-determining stage; meanwhile, the mass removal of adsorbate is well-thought-out a rapid process [33, 34].

From fitting Fig. 12a–c, we noticed that adsorption of Cr(VI) on surface of  $\text{BiFeO}_3\text{-Ni}_{0.1}\text{Fe}_{2.9}\text{O}_4$  nanocomposite was occurred through pseudo-second-order (Tables 4).

## 4 Conclusion

In this work, nanocomposites of  $\text{BiFeO}_3\text{-Ni}_{0.1}\text{Fe}_{2.9}\text{O}_4$  were prepared successfully by mixing two separate phase of  $\text{BiFeO}_3$  and  $\text{Ni}_{0.1}\text{Fe}_{2.9}\text{O}_4$ . The obtained nanocomposite shows good results for dielectric study as well as magnetic parameters values. Prepared nanocomposite was used for removal Cr(VI) from aqueous solution at various experimental parameters such as pH and contact time. The optimum conditions for adsorption were obtained at pH 6 after 40 min. Adsorption process of Cr (VI) was occurred through monolayer Langmuir adsorption and follows pseudo-second-order kinetics.



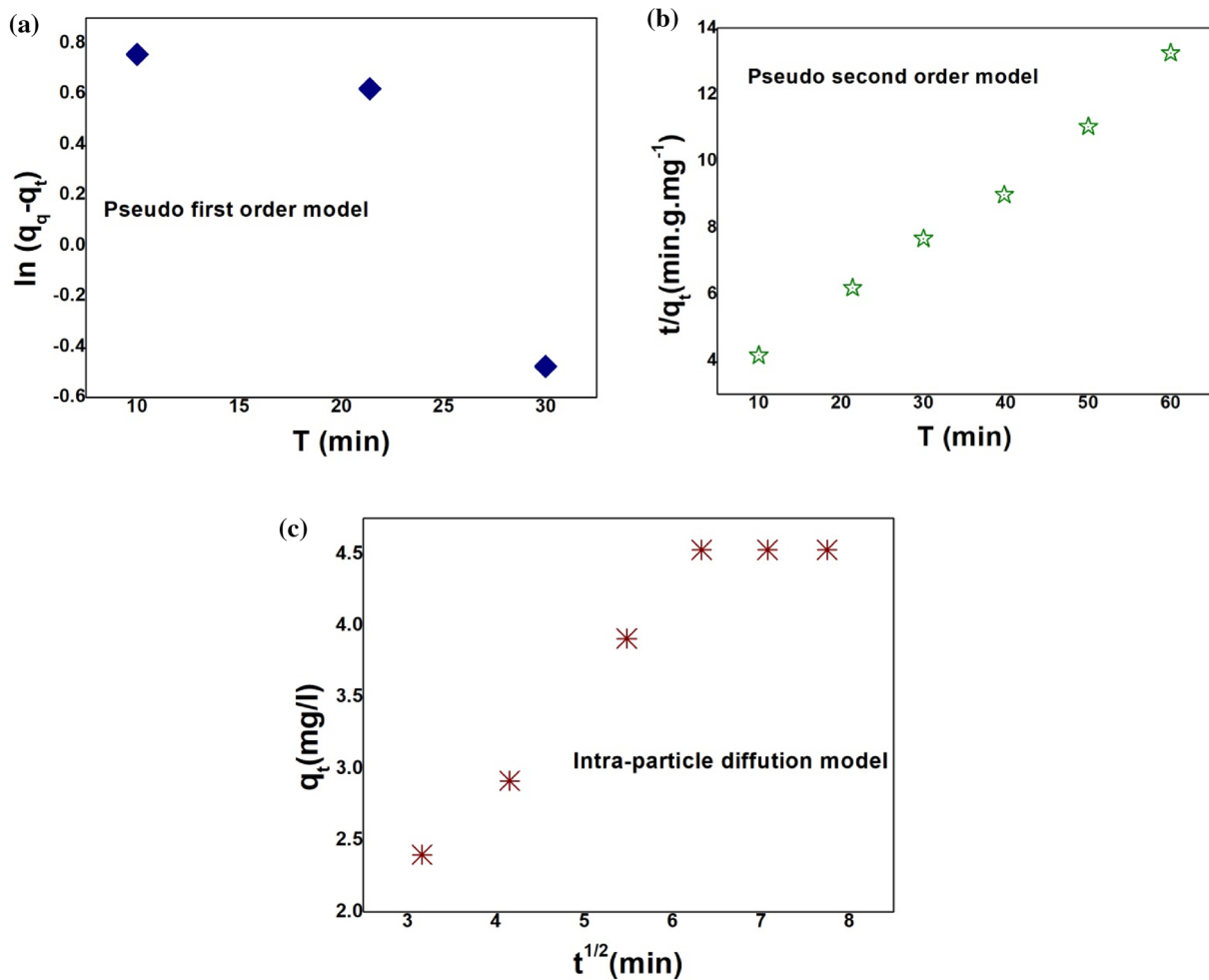


**Fig. 12** a Pseudo-first-order model, b pseudo-second-order model and c intra-particle diffusion model for BiFeO<sub>3</sub>-Ni<sub>0.1</sub>Fe<sub>2.9</sub>O<sub>4</sub> nanocomposite.

**Table 4** Comparison between this work and reported literature

Adsorbent	Adsorbate	Removal efficiency %	Refs.
Banana peel powder (BPP)	Cr(VI)	15	[34]
ZnO/Ce <sub>2</sub> O <sub>3</sub>	Cr(VI)	50	[35]
SiO <sub>2</sub> /Ce <sub>2</sub> O <sub>3</sub>	Cr(VI)	55	[35]
Nickel ferrite/titanium oxide magnetic nanocomposite	Cr(VI)	60	[36]
GO-SBA-15	Cr(VI)	9	[37]
BiFeO <sub>3</sub> -Ni <sub>0.1</sub> Fe <sub>2.9</sub> O <sub>4</sub> nanocomposite	Cr(VI)	75	This work

**Acknowledgements** The author extends her appreciation to the Cairo University.

**Authorship confirmation form manuscript title** Study the multiferroic properties of BiFeO<sub>3</sub>/Ni<sub>0.1</sub>Fe<sub>2.9</sub>O<sub>4</sub> for heavy metal removal. The author certifies that: the author has participated in (a) conception and design, or analysis and interpretation of the data; (b) drafting the article or

revising it critically for important intellectual content; and (c) approval of the final version. This manuscript has not been submitted to, nor is under review at, another journal or other publishing venue. The author has affiliation with organizations with direct or indirect financial interest in the subject matter discussed in the manuscript.

**Funding** Open access funding provided by The Science, Technology & Innovation Funding Authority (STDF) in cooperation with The Egyptian Knowledge Bank (EKB).

**Research data policy and data availability statements** Data sharing is not applicable to this article as no datasets were generated or analyzed during the current study.

## Declarations

**Conflict of interest** The author declares that she has no conflict of interests.

**Open Access** This article is licensed under a Creative Commons Attribution 4.0 International License, which permits use, sharing, adaptation, distribution and reproduction in any medium or format, as long as you give appropriate credit to the original author(s) and the source, provide a link to the Creative Commons licence, and indicate if changes

were made. The images or other third party material in this article are included in the article's Creative Commons licence, unless indicated otherwise in a credit line to the material. If material is not included in the article's Creative Commons licence and your intended use is not permitted by statutory regulation or exceeds the permitted use, you will need to obtain permission directly from the copyright holder. To view a copy of this licence, visit <http://creativecommons.org/licenses/by/4.0/>.

## References

- M. Fiebig, Revival of the magnetoelectric effect. *J. Phys. D Appl. Phys.* **38**, R123 (2005)
- S.-Y. Wang, X. Qiu, J. Gao, Y. Feng, W.N. Su, J.X. Zheng, D.J. Li, Electrical reliability and leakage mechanisms in highly resistive multiferroic La<sub>0.1</sub>Bi<sub>0.9</sub>FeO<sub>3</sub> ceramics. *Appl. Phys. Lett.* **98**, 152902 (2011)
- M.M. Arman, R. Ramadan, Optical, magnetic, and electrical studies of nanometric Bi<sub>1-x</sub>NdxFeO<sub>3</sub> Perovskite. *J. Supercond. Novel Magn.* (2020). <https://doi.org/10.1007/s10948-020-05441-1>
- P. Jubu, F. Yam, V. Igba, K. Beh, Tauc-plot scale and extrapolation effect on bandgap estimation from UV-vis-NIR data—a case study of  $\beta$ -Ga<sub>2</sub>O<sub>3</sub>. *J. Solid State Chem.* **290**, 1276 (2020)
- H. Liu, X.-X. Li, X.-Y. Liu, Z.-H. Ma, Z.-Y. Yin, W.-W. Yang, Y.-S. Yu, A DFT study on the detection of cathinone drug on the Au-decorated BC<sub>3</sub> nanosheet. *Rare Met.* **40**(4), 808–816 (2021)
- H. Imam, K. Elsayed, M.A. Ahmed, R. Ramdan, Effect of experimental parameters on the fabrication of gold nanoparticles via laser ablation. *Opt. Photon. J.* **2**, 73–84 (2012)
- X. Han, P. Tian, H. Pang, Q. Song, G. Ning, Y. Yu, H. Fang, Catalytic asymmetric synthesis of 3,3-disubstituted oxindoles: diazooxindole joins the field. *Rsc Adv.* **4**, 28119–28125 (2014)
- M.M. Arman, M.A. Ahmed, Effect of vacancy Co-doping on the structure, magnetic and dielectric properties of LaFeO<sub>3</sub> perovskite nanoparticles. *Appl. Phys. A* **128**, 1–9 (2022)
- M.A. Ahmed, S.T. Bishay, R. Ramadan, Water detoxification using gamma and alfa alumina nanoparticles prepared by micro emulsion route. *J. Nanosci. Nanotechnol.* **9**(2), 064–074 (2015)
- N.F. Mott, E.A. Davis, *The characterization and study of physical parameters of Ge modified Se-Sn-Pb chalcogenide system* (Clarendon, Oxford, 1979)
- D.L. Wood, J. Tauc, Spectroscopic studies of nanocomposites based on PEO/PVDF blend loaded by SWCNTs. *Phys. Rev. B* **5**, 3144 (1972)
- M. Reda, S.I. El-Deck, Improvement of ferroelectric properties via Zr doping in barium titanate nanoparticles. *J. Mater. Sci. Mater. Electron* **33**(21), 16753–16776 (2022)
- P. Mallick, S.K. Satpathy, B. Behera, Study of structural, dielectric, electrical, and magnetic properties of samarium-doped double perovskite material for thermistor applications. *Braz. J. Phys.* **52**(6), 1–15 (2022)
- E.E. Ateia, R. Ramadan, A.S. Shafaay, Efficient treatment of lead-containing wastewater by CoFe<sub>2</sub>O<sub>4</sub>/graphene nanocomposites nanocomposites. *Appl. Phys. A* **126**, 222 (2020). <https://doi.org/10.1007/s00339-020-3401-3>
- S.A. Al Kiey, R. Ramadan, M.M. El-Masry, Synthesis and characterization of mixed ternary transition metal ferrite nanoparticles comprising cobalt, copper and binary cobalt–copper for high-performance supercapacitor applications. *Appl. Phys. A* **128**, 473 (2022). <https://doi.org/10.1007/s00339-022-05590-1>
- D. Mohanty, A.U. Naik, P.K. Nayak, B. Behera, S.K. Satpathy, Electrical transport properties of layered structure bismuth oxide: Ba<sub>0.5</sub>Sr<sub>0.5</sub>Bi<sub>2</sub>V<sub>2</sub>O<sub>9</sub>. *J. Mater. Sci.: Mater. Electron* **25**, 117–123 (2021)
- E.E. Ateia, R. Ramadan, B. Hussein, Studies on multifunctional properties of GdFe<sub>1-x</sub>CoxO<sub>3</sub> multiferroics. *Appl. Phys. A* **126**, 340 (2020). <https://doi.org/10.1007/s00339-020-03518-1>
- S.K. Satpathy, N.K. Mohanty, A.K. Behera, B. Behera, Dielectric and electrical properties of 0.5 (BiGd<sub>0.05</sub>Fe<sub>0.95</sub>O<sub>3</sub>)-0.5 (PbZrO<sub>3</sub>) composite. *Mater. Sci. Pol.* **32**(1), 59–65 (2014)
- M. Fiebig, Th. Lottermoser, D. Fröhlich, A.V. Goltsev, R.V. Pisarev, Observation of coupled magnetic and electric domains. *Nat. (Lond.)* **419**, 818–820 (2002)
- R. Ramadan, N. Shehata, Adsorptive removal of methylene blue onto MFe<sub>2</sub>O<sub>4</sub>: kinetics and isotherm modeling. *Desalin. Water Treat.* **227**, 370–83 (2021)
- T.S. Tverdokhlebova, L.S. Antipina, V.L. Kudryavtseva, K.S. Stankevich, I.M. Kolesnik, E.A. Senokosova, E.A. Velikanova, L.V. Antonova, D.V. Vasilchenko, G.T. Dambaev, E.V. Plotnikov, V.M. Bouzник, E.N. Bolbasov, Composite ferroelectric membranes based on vinylidene fluoride-tetrafluoroethylene copolymer and polyvinylpyrrolidone for wound healing. *Membranes* **11**, 21 (2021)
- M.K. Rania Ramadan, Ahmed, Impact of adding vanadium pentoxide to Mn-doped magnetite for technological uses. *Appl. Phys. A* **128**, 1056 (2022). <https://doi.org/10.1007/s00339-022-06197-2>
- E.E. Ateia, A.A. Allah, R. Ramadan, Impact of GO on Non-stoichiometric Mg<sub>0.85</sub>K<sub>0.3</sub>Fe<sub>2</sub>O<sub>4</sub> ferrite nanoparticles. *J. Supercond. Novel Magn.* (2022). <https://doi.org/10.1007/s10948-022-06327-0>
- M.M. El-Masry, R. Ramadan, Enhancing the properties of PVDF/MFe<sub>2</sub>O<sub>4</sub>; (M: Co–Zn and Cu–Zn) nanocomposite for the piezoelectric optronic applications. *Mater. Electron. J. Mater. Sci.* (2022). <https://doi.org/10.1007/s10854-022-08493-2>
- R. Ramadan, A.M. Ismail, Tuning the physical properties of PVDF/PVC/Zinc ferrite nanocomposites films for more efficient adsorption of Cd (II). *J. Inorg. Organ. Polym. Mater.* (2022). <https://doi.org/10.1007/s10904-021-02176-x>
- M.A. Morales, I. Fernandez-Cervantes, R. Agustin-Serrano, S. Ruiz-Salgado, M.P. Sampedro, J.L. Varela-Caselis, R. Portillo, E. Rubio, Correction to “silver-doped cadmium selenide/graphene oxide-filled cellulose acetate nanocomposites for photocatalytic degradation of malachite green toward wastewater treatment.” *Res. Phys.* **12**, 1344–1356 (2019)
- S. Jana, S. Garain, S. Sen, D. Mandal, The influence of hydrogen bonding on the dielectric constant and the piezoelectric energy harvesting performance of hydrated metal salt mediated PVDF films. *Chem. Phys.* **17**(26), 17429–17436 (2015)
- M.K. Ahmed, R. Ramadan, S.I. El-dek, V. Uskokovic, *J. Alloys Compd.* **801**, 70–81 (2019)
- E.E. Ateia, D.E. El-Nashar, R. Ramadan, M.F. Shokry, Synthesis and characterization of EPDM/ferrite nanocomposites. *J. Inorg. Organomet. Poly. Mat.* **30**(4), 1041–1048 (2020)
- M.M. El-Masry, R. Ramadan, The effect of CoFe<sub>2</sub>O<sub>4</sub>, CuFe<sub>2</sub>O<sub>4</sub> and Cu/CoFe<sub>2</sub>O<sub>4</sub> nanoparticles on the optical properties and piezoelectric response of the PVDF polymer. *Appl. Phys. A* **128**, 110 (2022). <https://doi.org/10.1007/s00339-021-05238-6>
- T. Igarashi, P.H. Salgado, H. Uchiyama, H. Miyamae, N. Iyatomi, K. Hashimoto, A simple and efficient recovery technique for gold ions from ammonium thiosulfate medium by galvanic interactions of zero-valent aluminum and activated carbon: a parametric and mechanistic study of cementation. *Sci. Total. Environ.* **208**, 136877 (2020)
- S. Ikram, J. Jacob, K. Mahmood, A. Ali, N. Amin, U. Rehman, Effective removal of chromium from wastewater with Zn doped Ni ferrite nanoparticles produced using co-precipitation method. *Phys. B Condens. Matter* **580**, 411764 (2020)
- R. Jabbar, S.H. Sabeeh, A.M. Hameed, Cobalt-doped hydroxyapatite nanoparticles as a new eco-friendly catalyst of luminol–H<sub>2</sub>O<sub>2</sub> based chemiluminescence reaction: study of key factors,

- improvement the activity and analytical application. *J. Magn. Magn Mater.* **494**, 165726 (2020)
34. X. Gonze, B. Amadon, P.-M. Anglade, J.-M. Beuken, F. Bottin, P. Boulanger, F. Bruneval, D. Caliste, R. Caracas, M. Côté, Abinit: first-principles approach to material and nanosystem properties. *Comput. Phys. Commun.* **180**(12), 2582–2615 (2009). <https://doi.org/10.1016/j.cpc.2009.07.007>
35. R. Ramadan, M.M. El-Masry, Comparative study between CeO<sub>2</sub>/Zno and CeO<sub>2</sub>/SiO<sub>2</sub> nanocomposites for (Cr6+) heavy metal removal. *Appl. Phys. A* **127**, 876 (2021). <https://doi.org/10.1007/s00339-021-05037-z>
36. R. Jabbar, S.H. Sabeeh, A.M. Hameed, Structural, dielectric and magnetic properties of Mn+2 doped cobalt ferrite nanoparticles. *J. Magn. Magn. Mater.* **494**, 165726 (2020). <https://doi.org/10.1016/j.jmmm.2019.165726>
37. I.E. Kolesnikov, D.S. Kolokolov, M.A. Kurochkin, M.A. Voznesenskiy, M.G. Osmolowsky, E. Lähderanta, O.M. Osmolovskaya, Morphology and doping concentration effect on the luminescence properties of SnO<sub>2</sub>: Eu<sup>3+</sup> nanoparticles. *J. Alloys Compd.* **822**, 153640 (2020). <https://doi.org/10.1016/j.jallcom.2020.153640>

**Publisher's Note** Springer Nature remains neutral with regard to jurisdictional claims in published maps and institutional affiliations.